Facet-Dependent Selectivity of Cu Catalysts in Electrochemical CO_2 Reduction at Commercially Viable Current Densities

De Gregorio, Gian Luca; Burdyny, Thomas; Loiudice, Anna; Iyengar, Pranit; Smith, Wilson A.; Buonsanti, Raffaella

DOI
10.1021/acscatal.0c00297

Publication date
2020

Document Version
Final published version

ACS Catalysis

pubs.acs.org/acscatalysis

Research Article

Facet-Dependent Selectivity of Cu Catalysts in Electrochemical CO_2 Reduction at Commercially Viable Current Densities

Gian Luca De Gregorio, Thomas Burdyny, Anna Loiudice, Pranit Iyengar, Wilson A. Smith, and Raffaella Buonsanti*

Cite This: *ACS Catal.* 2020, 10, 4854−4862

Read Online

ACCESS | Metrics & More | Article Recommendations | Supporting Information

ABSTRACT: Despite substantial progress in the electrochemical conversion of CO_2 into value-added chemicals, the translation of fundamental studies into commercially relevant conditions requires additional efforts. Here, we study the catalytic properties of tailored Cu nanocatalysts under commercially relevant current densities in a gas-fed flow cell. We demonstrate that their facet-dependent selectivity is retained in this device configuration with the advantage of further suppressing hydrogen production and increasing the faradaic efficiencies toward the CO_2 reduction products compared to a conventional H-cell. The combined catalyst and system effects result in state-of-the art product selectivity at high current densities (in the range 100−300 mA/cm^2) and at relatively low applied potential (as low as −0.65 V vs RHE). Cu cubes reach an ethylene selectivity of up to 57% with a corresponding mass activity of 700 mA/mg, and Cu octahedra reach a methane selectivity of up to 51% with a corresponding mass activity of 1.45 A/mg in 1 M KOH.

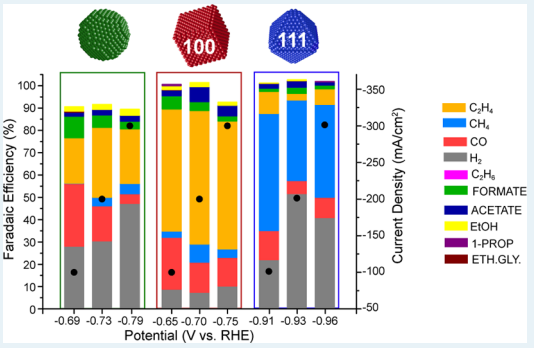

KEYWORDS: *electrochemical CO_2 reduction, nanocatalyst, structural selectivity, copper, gas-diffusion electrolyzer*

Although in the last decades several advances have been recorded in the field of renewable energy, these sources are discontinuous and the energy generated cannot easily be stored for long periods of time.[1−3] In this scenario, the electrochemical CO_2 reduction reaction (CO_2RR) represents an appealing process that can be conveniently integrated with various renewable energy systems for producing carbon-based chemical feedstocks and fuels.[4,5] However, this method must satisfy several requirements in order to become an economically valuable solution. At present, CO_2RR suffers from poor efficiency due to the CO_2 thermodynamic stability and to the reaction kinetic impediments, which result in the need for a large overpotential to activate and convert this molecule to more energy-dense products.[6−8]

Among the transition metals, copper is the only one capable of driving CO_2RR toward longer chain hydrocarbons and alcohols at reasonable faradaic efficiencies (FEs).[9−16] Several studies highlight that the obtained reduction products depend on multiple factors, including the environmental pH,[14,15] the nature of the electrolyte,[17−19] the applied potential,[10,20] the diffusion mechanism of CO_2,[21,22] as well as the chemical and morphological characteristics of the catalyst itself.[23,24] These conclusions have been mostly obtained by experiments performed in the traditional H-cell, where CO_2 is dissolved in an aqueous electrolyte (the most common being 0.1 M $KHCO_3$) and the catalysts are primarily deposited on flat glassy-carbon electrodes.[25] While these testing conditions can provide valuable information about the intrinsic activity of different catalytic materials, current densities are limited by the low catalyst loading allowed on the flat electrode and, more importantly, by the low solubility of CO_2 in water and the long CO_2 diffusion pathway to the catalyst surface.[21,22,26]

Recently, several studies have performed CO_2RR in gas-fed reactors capable of sustaining high current densities with acceptable faradaic efficiencies.[21,22,26,27] Using this approach, a very high surface area porous catalyst layer can be employed, so that CO_2 mass limitations to this surface are greatly reduced, resulting in substantially higher current densities at lower overall potentials.[28,29] Several architectures have been proposed and realized to achieve these goals, including flow cell configurations based on gas-diffusion electrodes (GDE).[26,30−32] With this design, conversion efficiencies for ethylene up to 70% at a potential of −0.55 V vs RHE (reversible hydrogen electrode) and current densities up to 300 mA/cm^2 have been reported in the presence of a highly concentrated alkaline electrolyte (10 M KOH).[33]

Received: January 18, 2020
Revised: March 8, 2020
Published: March 27, 2020

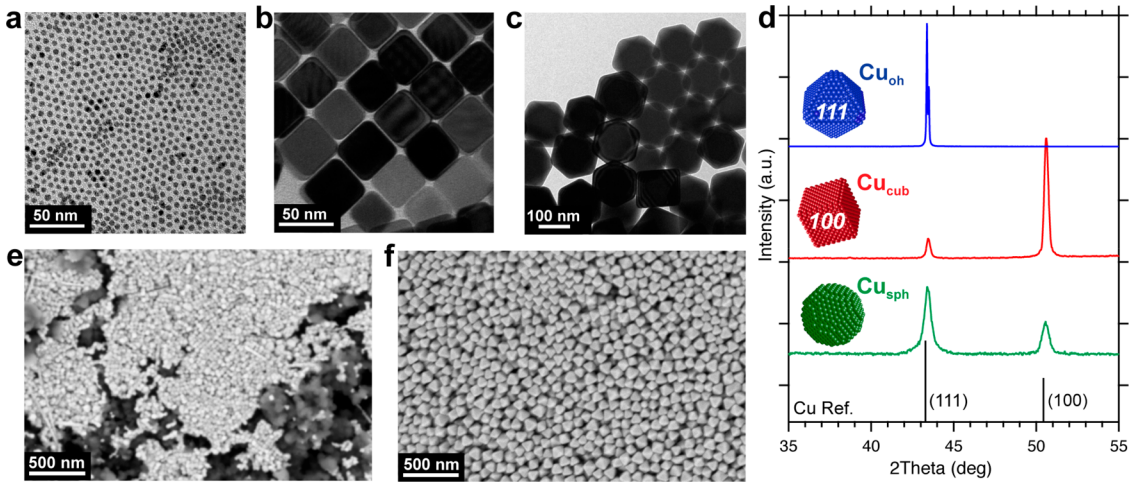

Figure 1. (a, b, and c) TEM images of the as-synthesized Cu_{sph}, Cu_{cub}, and Cu_{oh}, respectively. (d) XRD patterns of the obtained materials along with the Cu reference pattern (PDF no. 04-0836). (e and f) SEM images of Cu_{cub} (440 $\mu g/cm^2$) and Cu_{oh} (200 $\mu g/cm^2$) NCs which were spray-coated and drop-casted, respectively, on a Sigracet BC39 GDL.

Investigations on Cu single crystals in an H-cell have revealed that the (100) surface is more selective for C_2H_4, whereas the Cu (111) surface is more selective toward CH_4 under CO_2RR conditions.[34−37] Nanoparticle-based studies, including our own, have also demonstrated that such facet-dependent structural selectivity is maintained down to the nanoscale and can be further tuned through size effects.[38−42] Decade-long studies on nanocatalysts for the oxygen reduction reaction, however, have evidenced that tests under idealized conditions do not predict the catalytic activity and stability under conditions relevant for commercial-scale reactors.[43,44] For this reason, the impressive performance in fundamental studies has never been reproduced into a membrane electrode assembly used in fuel cells.[43,44]

When we consider the development of catalysts for CO_2 electrolysis, the intrinsic nature of the reaction warrants a similar degree of scepticism. In particular, in order to reach substantial current densities due to the mass transport limitations of CO_2 in aqueous electrolytes, a catalyst must be incorporated into either a GDE or a membrane electrode assembly. Under these conditions, the catalyst layer now functions as a porous electrode due to the electrolyte/ion pathway on one side of the catalyst and the CO_2 diffusion pathway on the other.[21] Such configurations are then expected to provide more surface area and reach higher current densities at lower applied potentials, which can impact not only potential-dependent product formation but also the restructuring and stability of facets on metal surfaces. Further, as current densities are increased, the reaction environment becomes substantially different from those achievable within controlled H-cell systems.[21] Indeed, multiphysical transport modeling of mesostructured silver electrodes has already shown that the improved selectivity toward CO compared to flat silver electrodes is purely a result of mass transport effects.[45] Similar effects to those described above could play a role when faceted Cu nanoparticles are integrated into a GDE. A recent study of (100) faceted Cu nanoparticles in alkaline gas diffusion electrolyzers has revealed that the systems were similarly selective toward ethylene as in an H cell.[46] Nevertheless, an increased local pH as a result of high current densities in a GDE would also promote formation of ethylene,[15,28,33] and so a definitive mechanism for the apparent similarity in selectivity is still not clear. Therefore, assessing various shaped Cu nanoparticles in different electrode architectures can help to provide further insights to the influences of surface facets, surface area, and the reaction environment on catalytic selectivity.

Having this in mind, we sought to directly compare the facet-dependent activity and selectivity of differently shaped Cu nanoparticles at much higher current densities than those achievable in an H-cell. By making this direct comparison, we can determine if the observed performance is maintained or altered in a GDE configuration compared to an aqueous H-cell and thus provide meaningful insights to the CO_2 reduction community that will shed light on an open debate.

Cu nanocrystals (NCs) of different shapes were synthesized according to colloidal methods previously reported by our group (see Experimental Section).[38,39,47] Figure 1 provides an overview of the morphological and structural characterization of the NCs. Figure 1a−c reports the transmission electron microscopy (TEM) images of the as-obtained Cu spheres of 6 nm (Cu_{sph}), Cu cubes of 44 nm (Cu_{cub}), and Cu octhaedra of 150 nm (Cu_{oh}), which all possess high uniformity in size and shape. These structures were chosen as they were found to be separately optimally selective for ethylene, methane, and a mixture of C_1−C_2 products, respectively, in H-cell tests.[38−42] X-ray diffraction (XRD) patterns in Figure 1d show the characteristic preferential orientation for the Cu_{cub} and Cu_{oh}, which is along the (100) and (111) directions, respectively, whereas the Cu_{sph}'s exhibit both orientations and a peak ratio closer to the bulk copper reference. More extensive characterization of the same NCs is reported in our previous work.[38,39,47] The as-synthesized NCs were spray-coated or drop-casted onto the GDL to form the gas diffusion electrode (GDE), as described in the Experimental Section. No particular difference was observed between the two deposition techniques upon optimization (Figure S1). Figure 1e and 1f reports representative in-plane scanning electron microscopy (SEM) images of the Cu_{cub} and Cu_{oh} NCs deposited on the GDL for the highest loadings used in this work, revealing a high degree of coverage.

The catalytic performance of the as-prepared GDEs was tested in a gas-fed flow cell with 1 M KOH as the supporting electrolyte (Experimental Section, Table S1). This setup was

https://dx.doi.org/10.1021/acscatal.0c00297
ACS Catal. 2020, 10, 4854−4862

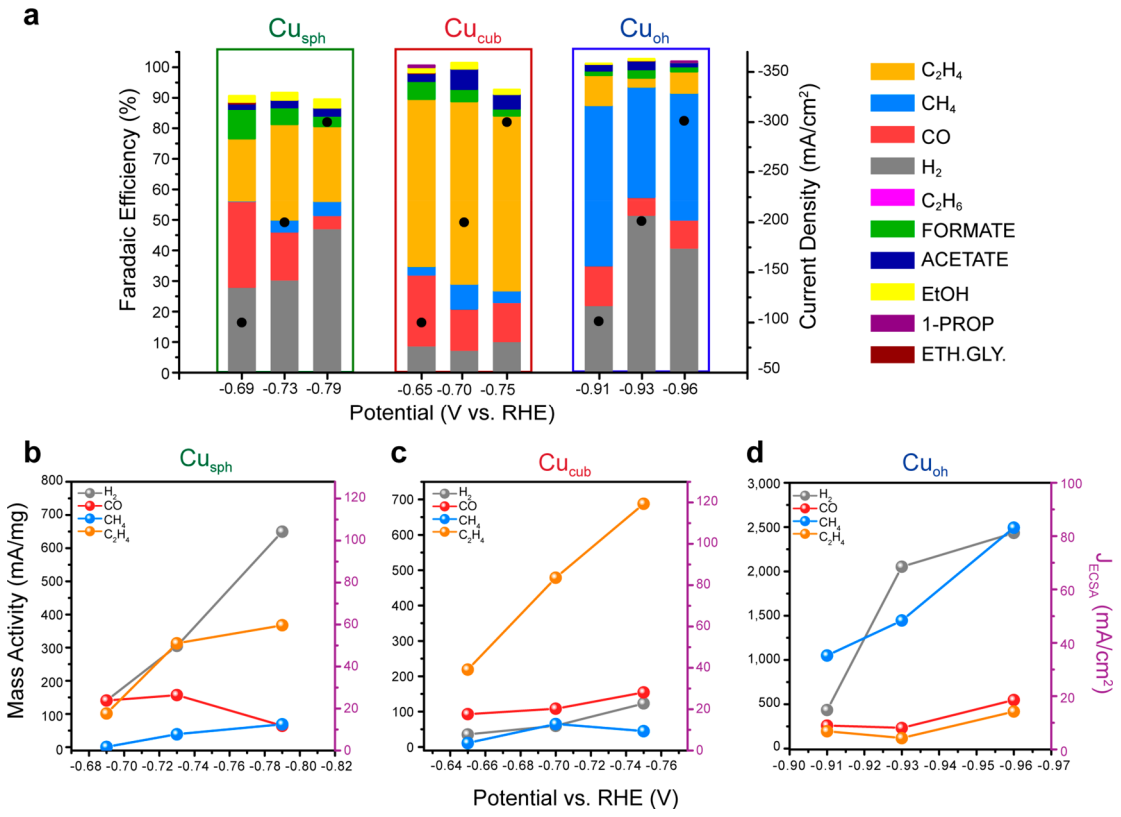

Figure 2. (a) Faradaic efficiencies vs potential for Cu_{sph} (200 $\mu g/cm^2$), Cu_{cub} (250 $\mu g/cm^2$), and Cu_{oh} (50 $\mu g/cm^2$) deposited on a GDL and measured in the gas-fed flow cell in 1 M KOH. These loadings were chosen to ensure similar catalyst coverage of the GDL, similar ECSA (Figure S2, Table S2), and conditions far from a mass transport-limited regime. Detailed discussion is reported in the SI. Black dots in a represent the geometric current density for each case (right axis). Higher values of current densities were not achievable with our current setup. (b–d) Mass activities (left axis) and partial current density normalized by the ECSA (right axis) for each of the detected gas products vs potential for the three NCs studied. All potentials are *iR* corrected (see SI for details).

reproduced from previous literature, and the alkaline electrolyte was chosen because of the reported record FE toward ethylene of 36% and 66% with partial current densities of 150 and 184 mA/cm^2 in KOH 1 and 10 M, respectively, at an applied potential of around −0.55 V vs RHE.[28,33] Figure 2 reports the faradaic efficiencies (FEs) obtained for the three NCs in the gas-fed flow cell along with the partial mass activities and current densities normalized by the electrochemically active surface area (ECSA) at three representative values of *iR*-corrected potentials. The current densities normalized by the geometric area are shown in Figure S3; the corresponding CO_2 conversion efficiency and cell voltages are reported in Figure S4.

At a current density of 100 mA/cm^2 at −0.69 V vs RHE, Cu_{sph} NCs produce 28% CO and 20% ethylene. At a higher current density (200 mA/cm^2, −0.79 V vs RHE), the FE for CO drops to 16%. Concomitantly, ethylene becomes the main CO_2RR reaction product (FE ≈ 31%), which suggests that more CO molecules undergo coupling. Finally, when the Cu_{sph}'s are investigated at 300 mA/cm^2 and −0.86 V vs RHE, HER increases (FE ≈ 43%), CO further decreases (FE ≈ 4%), as well as C_2H_4 decreases (FE ≈ 25%). The mass activities in Figure 2b follow the same described trend. Overall, the behavior of the Cu_{sph} (Figure 2a and 2b) resembles that of polycrystalline copper tested in a similar device configuration.[21,29−31,33]

When turning to the Cu_{cub}'s, they exhibit a much higher selectivity toward ethylene compared to the spheres across all of the potentials (Figure 2a). This result points at the fact that the exposed (100) facets do play a role in directing selectivity, even under these more extreme conditions. Specifically, conversion of CO_2 to C_2H_4 ranges from 55% at 100 mA/cm^2 and −0.65 V vs RHE to around 60% at 200 mA/cm^2 and −0.70 V vs RHE. Finally, at 300 mA/cm^2 and −0.75 V vs RHE, the observed conversion to ethylene is ∼57%. The corresponding ethylene mass activities are reported in Figure 2c and vary between 200 and 700 mA/mg, higher than the mass activities of the other products across the whole potential range. These efficiencies overcome those previously reported for randomly shaped Cu NCs in 1 M KOH, which were 36% at −0.58 V vs RHE at a similar ethylene partial geometric current density (150 mA/cm^2) and with lower ethylene mass activities of around 176 mA/mg.[28]

As for the Cu_{oh}'s, methane is the main hydrocarbon product, in line with the presence of the exposed (111) facets. The highest FE of ∼53% is obtained at 100 mA/cm^2 and −0.91 V vs RHE, with the corresponding lowest H_2 production (FE ≈ 22%). Ethylene is also present as a product but only with an ∼10% conversion efficiency at this current density, giving a methane:ethylene ratio of almost 5:1 compared to the roughly 1:20 ratio for the Cu_{cub}'s. At the higher current densities and potentials (200 mA/cm^2 and −0.93 V vs RHE; 300 mA/cm^2 and −0.96 V vs RHE), HER increases substantially and a general decrease of C_1 and C_2 products is observed, most likely due to the reaction entering a CO_2-depleted regime. Yet, methane does still remain the major CO_2RR product with FE

https://dx.doi.org/10.1021/acscatal.0c00297
ACS Catal. 2020, 10, 4854−4862

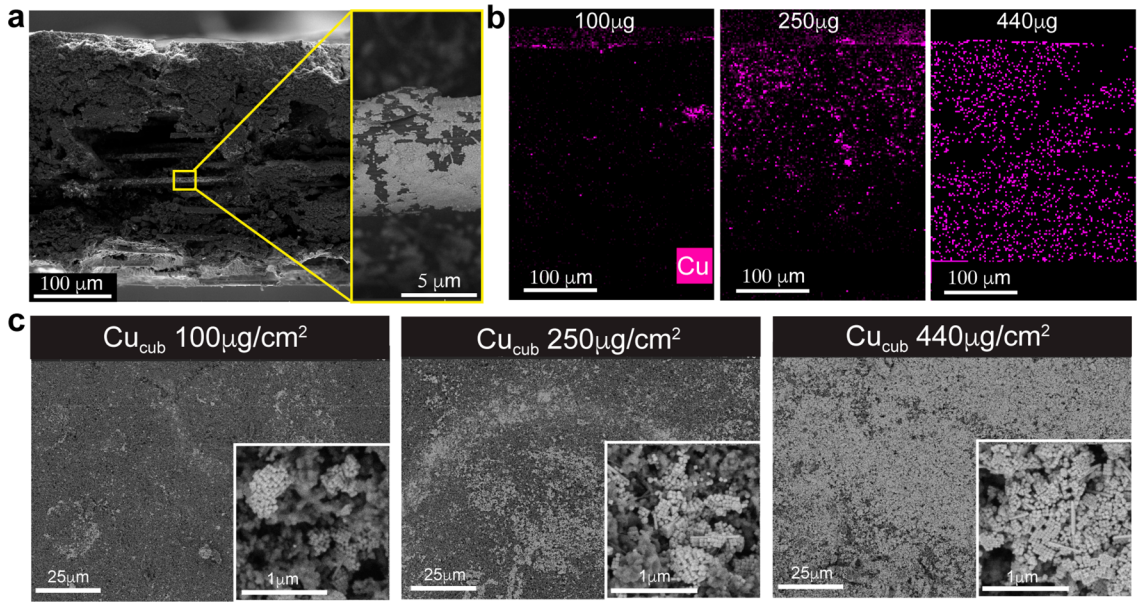

Figure 3. (a) Cross-sectional SEM images of 440 μg/cm^2 Cu$_{cub}$ NCs loaded on the GDL together with a magnification of the same. (b) EDX colored map cross-section of Cu$_{cub}$ for different loadings: 100, 250, and 440 μg/cm^2 from left to right. (c) In-plane SEM images of the samples in b with an inset of the same at higher magnification.

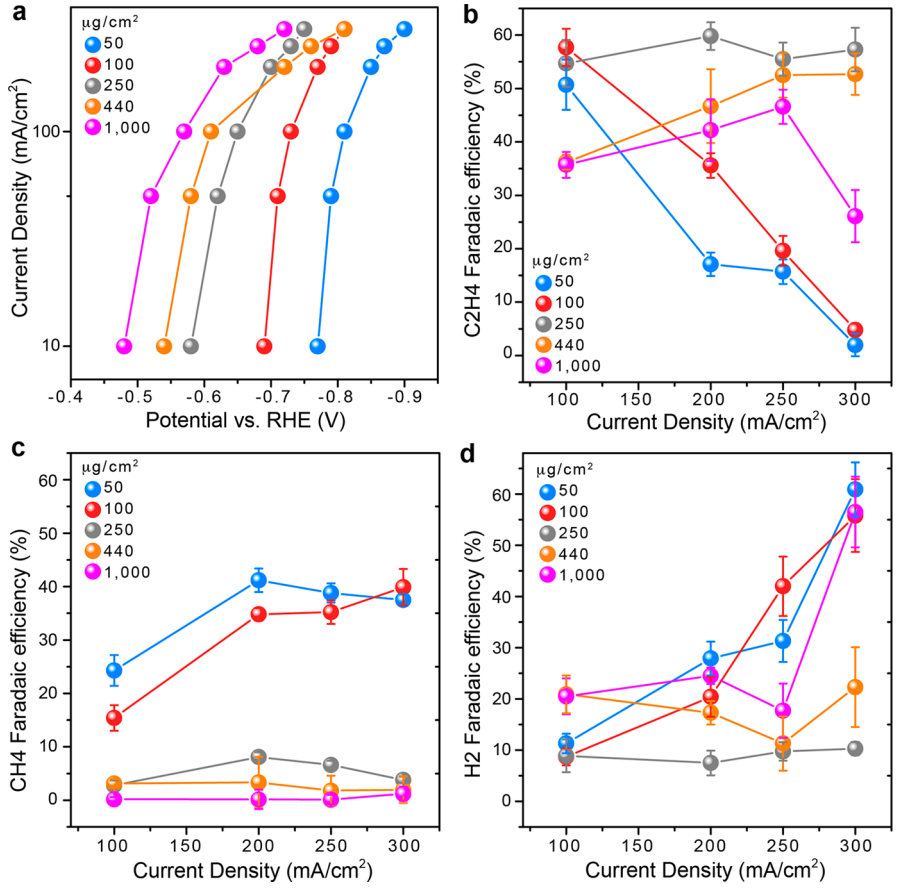

Figure 4. (a) Geometric current density vs *i*R-corrected potentials in 1.0 M KOH for Cu$_{cub}$ NCs on a GDL at varying loading. (b–d) Corresponding C_2H_4, CH_4, and H_2 faradaic efficiencies. Error bars indicate the standard deviation of three independent samples.

around 40%. The mass activities in Figure 2d are consistent with the selectivity trend, i.e., the methane and hydrogen current densities are higher than those for CO and ethylene across the whole potential range. To the best of our knowledge, the catalyst's mass activity toward methane is the largest reported to date and varies from 1.00 to 2.5 A/mg for potentials in the range from −0.91 to −0.96 V vs RHE.

https://dx.doi.org/10.1021/acscatal.0c00297
ACS Catal. 2020, 10, 4854−4862

Compared to the results obtained from the same NCs tested in an H-cell (Figure S5), the major CO_2RR products are preserved yet the hydrogen production is lower in the gas-fed flow cell at all potentials. The high alkaline conditions may explain this result as the CO_2 reduction reaction remains constant on the SHE scale while the hydrogen evolution reaction does not.[48] As CO_2 will interact with the alkaline electrolyte over time, it is also important to ensure that these changes do not impact the conclusions made over the length of the experiment.[49] For this reason, the pH of the bulk electrolyte was measured before and after the experiment as shown in Table S3. As the pH remains highly alkaline even at the end of the experiment, the slow degradation of the KOH electrolyte with CO_2 was not considered as a factor in these specific experiments.

Considering the notable differences in CH_4 vs C_2H_4 activity obtained with the faceted NCs, the following discussion will only focus on the Cu_{cub} and Cu_{oh} NCs and dive further into the influences of catalyst loading and operating conditions for these two catalysts.

Catalyst loading has been shown to affect the electrochemical performance due to the reconstruction of the deposited particles as well as by affecting transport at the mesoscale.[50,51] Furthermore, it is unknown whether the whole amount of catalyst loaded onto a GDL, or only part of it, reacts with CO_2.[21,33] For these reasons, it is important to investigate the effect of increasing catalyst loading on CO_2 depletion and availability while maximizing the electrochemically active surface area to reduce applied potentials. It is worth noting that reductive stripping of the native ligands from the catalyst surface occurs (Figure S6). Therefore, similar to what was concluded in comparative experiments done in an aqueous H-cell, the ligands do not have any major impact on the electrochemical performance.[52,53]

Figures 3, 4, and S7 summarize the results related to the effect of loading for the Cu_{cub}'s, while those for the Cu_{oh}'s are reported in the Supporting Information (Figures S8−S10). Figure 3a shows a representative cross-sectional SEM image for the Cu_{cub} NCs deposited on the GDL with a loading of 440 $\mu g/cm^2$, and Figure 3b illustrates the cross-section energy-dispersive X-ray spectroscopy (EDX) colored maps for the same NCs at different loadings. The images evidence that the as-deposited NCs are uniformly distributed through the whole GDL thickness as proved by the presence of a NC layer on the fibers of the backing paper support.

In Figure 3b, one can notice that a surface layer builds up on the top of the GDL. Figure 3c shows the top-down SEM images of Cu_{cub}NCs with the same loadings of Figure 3b. As the loading increases, the Cu_{cub}'s form an increasingly more compact layer on the top of the GDL. Very similar observations were made for the Cu_{oh}NCs, though formation of such a compact top layer occurred at lower loadings (200 $\mu g/cm^2$) than the Cu_{cub}NCs (440 $\mu g/cm^2$), most likely because of the bigger NC size (Figuress S8 and S9).

The CO_2RR performance of the Cu_{oh} and of the Cu_{cub} NCs was evaluated at loadings in the range of 50−1000 $\mu g/cm^2$ (Figures 4, S7, S10, and S11 and Tables S4 and S5). Figure 4a shows that the required potential can be driven down at higher loading as the catalytic surface area increases. At lower current densities, the Cu_{cub}NCs exhibit similar slopes for all loadings, indicative of a similar level of intrinsic activity. As the current increases above 100 mA/cm^2, the slope also changes. Such change is more pronounced for 440 and 1000 $\mu g/cm^2$, which are higher loadings than those utilized in Figure 2 (250 $\mu g/cm^2$). The deviation from a linear dependence of the current density on the potential in this high-current/high-loading region is likely a combined result of mass transport effects and changes in overall activity due to modifications of the local environment. Similar observations were made for the Cu_{oh} (Figure S10), though with even more drastic effects. Indeed, above 200 $\mu g/cm^2$, which is when the thick top layer forms, only vigorous gas bubbling from hydrogen production was observed on the GDE surface (Figures S8 and S9).

To gain further understanding about the accessibility of the electrolyte to the NCs, EDX analysis of the potassium through the GDE thickness was performed (Figure S12). It is reasonable to assume that the presence of potassium indicates a wetted electrode and that, therefore, all of the NCs are in the condition to be potentially active. We found that the increasing loading is accompanied by a decreasing concentration of potassium in the GDE up to the point of not detecting any potassium inside when the top compact layer forms. These results suggest that the top compact layer effectively prevents the electrolytes from penetrating into the pores, thus effectively impeding the reaction between CO_2 and water.

In agreement with this compositional analysis, the ECSA for the Cu_{cub} notably increases with a loading of up to 440 $\mu g/cm^2$ while the change becomes less significant between 440 and 1000 $\mu g/cm^2$ (Figure S2). Instead, the results for the Cu_{oh} evidence that 50 $\mu g/cm^2$ is already enough to maximize the active surface area, which we speculatively assign to the bigger size of the octahedra (Figure S2).

When analyzing the product selectivities at different loadings (Figure 4b−d), the FEs of the intermediate loadings (250 and 440 $\mu g/cm^2$) show an overall more moderate potential dependence. On the contrary, for the lower and higher loadings (50, 100, and 1000 $\mu g/cm^2$), the FE_{C2H4} and FE_{H2} decrease and increase, respectively, while going from lower to higher potentials (Figure 4b−d). For the samples with the lower loading, the HER increase is accompanied by increased methane as well (Figure 4d).

In order to explain the observed product distribution, various effects need to be considered. First, there are the aforementioned mass transport resistances. For the 1000 $\mu g/cm^2$ sample, the increased HER and decreased ethylene can be justified in terms of mass transport limitations, causing CO_2RR to be replaced with HER as current densities increase. Nevertheless, between 200 and 250 mA/cm^2 HER slightly decreases for both 440 and 1000 $\mu g/cm^2$, while polarization curves show already a decreasing slope. Thus, mass transport limitations cannot be the only explanation. Mass transport limitations also do not explain the increased CH_4 at higher potential for the lower loadings.

One could then consider the effect of polarization. It has been reported that at high overpotentials (<−0.8 V vs RHE), C_2H_4 and CH_4 can form simultaneously from the common intermediate *COH on both Cu (100) and Cu (111) facets.[15,34,35] This behavior however has not been observed during experiments in alkaline media.[15,54,55] We speculate that the negative potential applied to the system to meet the set current density at such low catalyst loadings (lesser exposed surface area) makes CH_4 more favorable than C_2H_4 at these potentials. However, polarization effects do not justify the high methane production of the 100 $\mu g/cm^2$ compared to the 250 and 440 $\mu g/cm^2$ for similar applied potentials (−0.77 V for

https://dx.doi.org/10.1021/acscatal.0c00297
ACS Catal. 2020, 10, 4854−4862

200 mA/cm^2, −0.75 V for 300 mA/cm^2, and −0.76 V for 250 mA/cm^2).

If we plot the FEs versus the applied potential (Figure S13), it becomes clear that another factor to consider is the optimal electrode potential range for a given product, which indeed changes for different loadings. These data contribute to explain the observations above. Finally, the contribution of the GDL itself to the high hydrogen evolution rate (FE ≈ 60%) in the low loadings may be considered as well (Figure S14).

The same effects (i.e., mass transport limitations, polarization effects, optimal potential range, substrate effects) explain the observed behavior for different loadings of Cu_{oh}NCs (Figure S13).

Finally, catalyst and device stability is as important as activity and selectivity. TEM and XRD analyses show that the morphological stability of the Cu_{cub} is preserved up to 6 h, and it is accompanied by stable ethylene production (Figures S15 and S16). These initial data point at an improvement of the intrinsic stability compared to what we previously observed in an H-cell.[52] The lower potentials needed in the gas-fed flow cell (−0.76/−0.65 V vs RHE with respect to the −1.1 V vs RHE in the H-cell) are one possible reason for the observed behavior. On the contrary, Cu_{oh} did not show high stability (Figures S17 and S18). In the case of the more stable Cu_{cub}, after 6 h, the entire device stops operating because of GDL flooding, thus suggesting that engineering solutions to achieve device stability for a longer time are crucial before continuing to further investigate the parameters contributing to catalyst stability.[21,56,57]

In summary, this study presents the integration of colloidally synthesized NCs in a gas-fed flow cell with optimal morphologies for high ethylene and methane conversion efficiencies and production rates. We observed that the Cu_{cub} NCs are highly selective toward C_2H_4, Cu_{oh} are selective toward CH_4, and Cu_{sph} are not selective toward any specific product. Loading experiments demonstrated that an optimal amount of catalyst must be deposited in order to achieve the best performance in terms of activity and selectivity. In particular, the catalyst layer should uniformly cover the GDL without clogging the porous structure. The latter results in a limited mass diffusion operational regime and promotes the subsequent evolution of hydrogen. Future modeling will help to understand mass transport in more detail.[45,58]

Overall, integration of the Cu NCs in the gas-fed flow electrolyzer enabled achievement of remarkable performance for ethylene and methane in a low-concentration alkaline electrolyte. Initial tests have revealed that these selectivities are preserved also in different electrolytes (Figure S19, Tables S6 and S7). Specifically, ethylene mass activities between 200 and 700 mA/mg in a potential range between −0.65 and −0.75 V vs RHE with a selectivity of ∼57% were obtained in 1 M KOH. The methane current densities were exceptionally large and varied from 1.45 to 2.5 A/mg in the potential range from −0.93 to −0.96 V vs RHE with selectivities between 51% and 41% in 1 M KOH. The latter is a very interesting fundamental result which illustrates the power of catalyst design even in gas-fed electrolyzers, as activity toward methane is expected and has generally been shown to be suppressed under high bulk and local pH conditions.[15,28,33]

■ ASSOCIATED CONTENT

Supporting Information

The Supporting Information is available free of charge at https://pubs.acs.org/doi/10.1021/acscatal.0c00297.

Experimental Section; sketch of the gas-fed flow cell used in this work and schematic representation of the NC-based GDE; in-plane SEM images of Cu_{oh} NCs drop casted and spray coated with a loading of 100 μg/cm^2; faradaic efficiency for the Cu_{sph}, Cu_{cub}, and Cu_{oh} NCs in the gas-fed flow cell; cyclic voltammetry at different scan rates on Cu_{oh} 50 μg/cm^2 in $KHCO_3$ 0.1 M, plot of capacitive current vs scan rate for Cu_{oh} 50 μg/cm^2, Cu_{cub} 250 μg/cm^2, and Cu_{sph} 200 μg/cm^2, and estimated ECSA vs NCs loading for Cu_{cub} and Cu_{oh}; roughness factors and electroactive area for different Cu samples; partial current densities normalized by the geometric area vs potential for Cu_{sph} (200 μg/cm^2), Cu_{cub} (250 μg/cm^2), and Cu_{oh} (50 μg/cm^2) measured in 1 M KOH; faradaic efficiencies and total CO_2 consumption versus the applied cell voltage; bulk pH values measured before and after the electrochemical measurements for the three NCs tested in 1 M KOH; faradaic efficiencies for Cu_{sph}, Cu_{cub}, and Cu_{oh} NCs measured in the H cell at different potentials, and comparison of CO_2RR vs HER selectivity for the three NCs measured at different potentials in the H cell and in the flow cell; FTIR analysis performed on the GDE before and after the chronopotentiometric measurements; faradaic efficiencies in 1.0 M KOH for Cu_{cub} NCs at different loadings at 100, 200, and 300 mA/cm^2 current densities, and highlight of the liquid products; in-plane SEM images of the Cu_{oh} NCs deposited on the GDL at different loadings; cross-section SEM images of Cu_{oh} NCs GDE at 200 μg/cm^2 loading at different magnifications, cross-section EDX map of the copper element, in-plane and cross-section SEM-EDX images for the 1 mg/cm^2 Cu_{oh} NCs loading, and corresponding cross-section SEM-EDX images; faradaic efficiencies in 1.0 M KOH for Cu_{oh} NCs at different loadings at 100, 200 and 300 mA/cm^2 current densities, geometric current density as a function of applied potential in 1.0 M KOH electrolyte for Cu_{oh} NCs at varying loadings, CH_4, H_2, C_2H_4, and CO faradaic efficiencies in 1.0 M KOH for Cu_{oh} NCs at different loadings in the current density range 100−300 mA/cm^2; FEs vs *iR*-corrected potential for different loadings of Cu_{oh}; linear plots of geometric current density as a function of applied potential in 1.0 M KOH electrolyte for Cu_{cub} NCs and Cu_{oh} NCs at varying loadings; cross-section SEM of the GDE loaded with different amounts of Cu_{cub} NCs, and EDX spectra in the energy range of the potassium peak; CH_4, C_2H_4, and H_2 faradaic efficiencies vs *iR*-corrected potentials for different loadings of Cu_{cub}; CH_4, C_2H_4, and H_2 faradaic efficiencies vs *iR*-corrected potentials for different loadings of Cu_{oh}; carbon GDL substrate measured in 1.0 M KOH at different applied currents; faradaic efficiency for the Cu_{cub} and Cu_{oh} NCs in the gas-fed flow cell in 1.0 M KOH at different applied currents and different loadings; applied potentials and mass activities for the Cu_{cub} and Cu_{oh} NCs in the gas-fed flow cell in 1.0 M KOH at different loadings; ethylene faradaic efficiency for Cu_{cub} NCs tested in the flow cell at

https://dx.doi.org/10.1021/acscatal.0c00297
ACS Catal. 2020, 10, 4854−4862

−100 mA/cm^2 in 1M KOH electrolyte, TEM images of the Cu_{cub} NCs tested in the H cell and in the flow cell after 3 and 6 h of operation, electrochemical testing for the H cell was performed at −1.1 V vs RHE in 0.1 M $KHCO_3$, SEM image Cu_{cub} NCs after 6 h of operation in the flow cell, and XRD patterns of Cu_{cub} NCs as prepared and after 3 h operation in the flow cell; stability of FE for the Cu_{cub} NCs at −300 mA/cm^2 in KOH, and SEM and TEM images of the same; SEM images of Cu_{oh} NCs at different applied voltages in 1.0 M KOH after 60 min of testing; faradaic efficiencies of Cu_{oh} NCs over time; faradaic efficiencies in 1.0 M KOH, 1.2 M KCl, and $KHCO_3$ 1.2 M, and Cu_{cub} and Cu_{oh} NCs together with the corresponding *iR*-corrected potential; faradaic efficiency for the Cu_{cub} and Cu_{oh} NCs in the gas-fed flow cell in 1.2 M KCl and 1.2 M $KHCO_3$ at different applied currents; bulk pH values measured before and after the electrochemical measurements for the three NCs tested in different electrolytes; additional references (PDF)

AUTHOR INFORMATION

Corresponding Author

Raffaella Buonsanti − *Laboratory of Nanochemistry for Energy, Institute of Chemical Sciences and Engineering, Ecole Politechnique Federale de Lausanne, Sion CH-1950, Switzerland*; orcid.org/0000-0002-6592-1869; Email: raffaella.buonsanti@epfl.ch

Authors

Gian Luca De Gregorio − *Laboratory of Nanochemistry for Energy, Institute of Chemical Sciences and Engineering, Ecole Politechnique Federale de Lausanne, Sion CH-1950, Switzerland*

Thomas Burdyny − *Materials for Energy Conversion and Storage, Department of Chemical Engineering, Delft University of Technology, Delft 2629 HZ, Netherlands*

Anna Loiudice − *Laboratory of Nanochemistry for Energy, Institute of Chemical Sciences and Engineering, Ecole Politechnique Federale de Lausanne, Sion CH-1950, Switzerland*

Pranit Iyengar − *Laboratory of Nanochemistry for Energy, Institute of Chemical Sciences and Engineering, Ecole Politechnique Federale de Lausanne, Sion CH-1950, Switzerland*

Wilson A. Smith − *Materials for Energy Conversion and Storage, Department of Chemical Engineering, Delft University of Technology, Delft 2629 HZ, Netherlands*

Complete contact information is available at: https://pubs.acs.org/10.1021/acscatal.0c00297

Author Contributions

G.L.D. designed and carried out all of the experiments and analyzed the data. T.B. provided assistance in the electrochemical experiments and data analysis. A.L. performed the XRD, SEM, TEM experiments and analyzed the data. P.I. synthesized the Cu_{oh} nanocrystals. W.A.S. contributed to discussion and supervision. R.B. designed and supervised the entire project. All authors discussed the results and assisted during manuscript preparation.

Notes

The authors declare no competing financial interest.

ACKNOWLEDGMENTS

R.B. acknowledges funding from the European Research Council (ERC) under the European Union's Horizon 2020 research and innovation program (grant agreement no. 715634-HYCAT). W.A.S. acknowledges funding from the European Research Council (ERC) under the European Union's Horizon 2020 research and innovation program (grant agreement no. 759743-WUTANG). P.I. was financially supported by Gaznat S.A. The authors thank Seyedeh Behnaz Varandili for performing inductively coupled plasma-optical emission spectroscopy (ICP-OES) measurements to determine sample concentration.

REFERENCES

(1) Chu, S.; Cui, Y.; Liu, N. The path towards sustainable energy. *Nat. Mater.* **2017**, *16*, 16.

(2) Kondratenko, E.-V.; Mul, G.; Baltrusaitis, J.; Larrazabal, G. O.; Perez-Ramırez, J. Status and perspectives of CO2 conversion into fuels and chemicals by catalytic, photocatalytic and electrocatalytic processes. *Energy Environ. Sci.* **2013**, *6*, 3112.

(3) Yang, Z.; Zhang, J.; Kintner-Meyer, M. C. W.; Lu, X.; Choi, D.; Lemmon, J. P.; Liu, J. Electrochemical Energy Storage for Green Grid. *Chem. Rev.* **2011**, *111*, 3577.

(4) De Luna, P.; Hahn, C.; Higgins, D.; Jaffer, S. A.; Jaramillo, T. F.; Sargent, E. H. What would it take for renewably powered electrosynthesis to displace petrochemical processes? *Science* **2019**, *364*, eaav3506.

(5) Vasileff, A.; Zheng, Y.; Qiao, S. Z. Carbon Solving Carbon's Problems: Recent Progress of Nanostructured Carbon□Based Catalysts for the Electrochemical Reduction of CO2. *Adv. Energy Mater.* **2017**, *7*, 1700759.

(6) Dutta, A.; Rahaman, M.; Luedi, N. C.; Mohos, M.; Broekmann, P. Morphology Matters: Tuning the Product Distribution of CO2 Electroreduction on Oxide-Derived Cu Foam Catalysts. *ACS Catal.* **2016**, *6*, 3804.

(7) Mistry, H.; Varela, A. S.; Bonifacio, C. S.; Zegkinoglou, I.; Sinev, I.; Choi, Y.-W.; Kisslinger, K.; Stach, E. A.; Yang, J. C.; Strasser, P.; Cuenya, B. R. Highly selective plasma-activated copper catalysts for carbon dioxide reduction to ethylene. *Nat. Commun.* **2016**, *7*, 12123.

(8) Roberts, F. S.; Kuhl, K. P.; Nilsson, A. High selectivity for ethylene from carbon dioxide reduction over copper nanocube electrocatalysts. *Angew. Chem., Int. Ed.* **2015**, *54*, 5179.

(9) Bagger, A.; Ju, W.; Varela, A. S.; Strasser, P.; Rossmeisl, J. Rossmeisl, Electrochemical CO2 Reduction: A Classification Problem. *ChemPhysChem* **2017**, *18*, 3266.

(10) Kuhl, K. P.; Cave, E. R.; Abram, D. N.; Jaramillo, T. F. New insights into the electrochemical reduction of carbon dioxide on metallic copper surfaces. *Energy Environ. Sci.* **2012**, *5*, 7050.

(11) Peterson, A. A.; Abild-Pedersen, F.; Studt, F.; Rossmeisl, J.; Nørskov, J. K. How copper catalyzes the electroreduction of carbon dioxide into hydrocarbon fuels. *Energy Environ. Sci.* **2010**, *3*, 1311.

(12) Hori, Y.; Wakebe, H.; Tsukamoto, T.; Koga, O. Electrocatalytic process of CO selectivity in electrochemical reduction of CO2 at metal electrodes in aqueous media. *Electrochim. Acta* **1994**, *39*, 1833.

(13) Hori, Y.; Kikuchi, K.; Suzuki, S. Production of CO and CH4 in electrochemical reduction of CO2 at metal electrodes in aqueous hydrogencarbonate solution. *Chem. Lett.* **1985**, *14*, 1695.

(14) Liu, X.; Schlexer, P.; Xiao, J.; Ji, Y.; Wang, L.; Sandberg, R. B.; Tang, M.; Brown, K. S.; Peng, H.; Ringe, S.; Hahn, C.; Jaramillo, T. F.; Nørskov, J. K.; Chan, K. pH effects on the electrochemical reduction of CO2 towards C2 products on stepped copper. *Nat. Commun.* **2019**, *10*, 32.

(15) Schouten, K. J. P.; Pérez-Gallent, E.; Koper, M. T. M. The influence of pH on the reduction of CO and CO2 to hydrocarbons on copper electrodes. *J. Electroanal. Chem.* **2014**, *716*, 53.

(16) Nitopi, S.; Bertheussen, E.; Scott, S. B.; Liu, X.; Engstfeld, A. K.; Horch, S.; Seger, B.; Stephens, I. E. L.; Chan, K.; Hahn, C.; Nørskov,

J. K.; Jaramillo, T. F.; Chorkendorff, I. Progress and Perspectives of Electrochemical CO2 Reduction on Copper in Aqueous Electrolyte. *Chem. Rev.* **2019**, *119* (12), 7610.
(17) Gao, D.; McCrum, I. T.; Deo, S.; Choi, Y.-W.; Scholten, F.; Wan, W.; Chen, J. G.; Janik, M. J.; Roldan-Cuenya, B. Activity and Selectivity Control in CO2 Electroreduction to Multicarbon Products over CuOx Catalysts via Electrolyte Design. *ACS Catal.* **2018**, *8*, 10012.
(18) Resasco, J.; Chen, L. D.; Clark, E.; Tsai, C.; Hahn, C.; Jaramillo, T. F.; Chan, K.; Bell, A. T. Promoter Effects of Alkali Metal Cations on the Electrochemical Reduction of Carbon Dioxide. *J. Am. Chem. Soc.* **2017**, *139*, 11277.
(19) Lum, Y.; Yue, B.; Lobaccaro, P.; Bell, A. T.; Ager, J. W. Optimizing C−C Coupling on Oxide-Derived Copper Catalysts for Electrochemical CO2 Reduction. *J. Phys. Chem. C* **2017**, *121*, 14191.
(20) Hori, Y.; Takahashi, R.; Yoshinami, Y.; Murata, A. Electrochemical Reduction of CO at a Copper Electrode. *J. Phys. Chem. B* **1997**, *101*, 7075.
(21) Burdyny, T.; Smith, W. A. CO2 reduction on gas-diffusion electrodes and why catalytic performance must be assessed at commercially-relevant conditions. *Energy Environ. Sci.* **2019**, *12*, 1442.
(22) Higgins, D.; Hahn, C.; Xiang, C.; Jaramillo, T. F.; Weber, A. Z. Gas-Diffusion Electrodes for Carbon Dioxide Reduction: A New Paradigm. *ACS Energy Lett.* **2019**, *4*, 317.
(23) Mistry, H.; Varela, A. S.; Kuhl, S.; Strasser, P.; Roldan-Cuenya, B. Nanostructured electrocatalysts with tunable activity and selectivity. *Nat. Rev. Mater.* **2016**, *1*, 16009.
(24) Tang, W.; Peterson, A. A.; Varela, A. S.; Jovanov, Z. P.; Bech, L.; Durand, W. J.; Dahl, S.; Nørskov, J. K.; Chorkendorff, I. The importance of surface morphology in controlling the selectivity of polycrystalline copper for CO2 electroreduction. *Phys. Chem. Chem. Phys.* **2012**, *14*, 76.
(25) Lobaccaro, P.; Singh, M. R.; Clark, E. L.; Kwon, Y.; Bell, A. T.; Ager, J. W. Effects of temperature and gas−liquid mass transfer on the operation of small electrochemical cells for the quantitative evaluation of CO2 reduction electrocatalysts. *Phys. Chem. Chem. Phys.* **2016**, *18*, 26777.
(26) Weekes, D. M.; Salvatore, D. A.; Reyes, A.; Huang, A.; Berlinguette, C. P. Electrolytic CO2 Reduction in a Flow Cell. *Acc. Chem. Res.* **2018**, *51*, 910.
(27) Min, S.; Yang, X.; Lu, A. Y.; Tseng, C. C.; Hedhili, M. N.; Li, L. J.; Huang, K. W. Low overpotential and high current CO2 reduction with surface reconstructed Cu foam electrodes. *Nano Energy* **2016**, *27*, 121.
(28) Ma, S.; Sadakiyo, M.; Luo, R.; Heima, M.; Yamauchi, M.; Kenis, P. J. A. One-step electrosynthesis of ethylene and ethanol from CO2 in an alkaline electrolyzer. *J. Power Sources* **2016**, *301*, 219.
(29) Brushett, F. R.; Zhou, W.-P.; Jayashree, R. S.; Kenis, P. J. A. Alkaline Microfluidic Hydrogen-Oxygen Fuel Cell as a Cathode Characterization Platform. *J. Electrochem. Soc.* **2009**, *156* (5), B565.
(30) Lee, W.; Kim, Y. E.; Youn, M. H.; Jeong, S. K.; Park, K. T. Catholyte-Free Electrocatalytic CO2 Reduction to Formate. *Angew. Chem., Int. Ed.* **2018**, *57*, 6883.
(31) Salvatore, D. A.; Weekes, D. M.; He, J.; Dettelbach, K. E.; Li, Y. C.; Mallouk, T. E.; Berlinguette, C. P. Electrolysis of Gaseous CO2 to CO in a Flow Cell with a Bipolar Membrane. *ACS Energy Lett.* **2018**, *3*, 149.
(32) Moller, T.; Ju, W.; Bagger, A.; Wang, X.; Luo, F.; Ngo Thanh, T.; Varela, A. S.; Rossmeisl, J.; Strasser, P. Efficient CO2 to CO electrolysis on solid Ni−N−C catalysts at industrial current densities. *Energy Environ. Sci.* **2019**, *12*, 640.
(33) Dinh, C.; Burdyny, T.; Kibria, M. G.; Seifitokaldani, A.; Gabardo, C. M.; García de Arquer, F. P.; Kiani, A.; Edwards, J. P.; De Luna, P.; Bushuyev, O. S.; et al. CO2 electroreduction to ethylene via hydroxide-mediated copper catalysis at an abrupt interface. *Science* **2018**, *360*, 783.
(34) Jiang, K.; Sandberg, R. B.; Akey, A. J.; Liu, X.; Bell, D. C.; Nørskov, J. K.; Chan, K.; Wang, H. Metal ion cycling of Cu foil for selective C−C coupling in electrochemical CO2 reduction. *Nat. Catal.* **2018**, *1*, 111.
(35) Schouten, K. J. P.; Qin, Z.; Perez Gallent, E.; Koper, M. T. M. Two pathways for the formation of ethylene in CO reduction on single-crystal copper electrodes. *J. Am. Chem. Soc.* **2012**, *134*, 9864.
(36) Schouten, K. J. P.; Pérez Gallent, E.; Koper, M. T. M. Structure Sensitivity of the Electrochemical Reduction of Carbon Monoxide on Copper Single Crystals. *ACS Catal.* **2013**, *3*, 1292.
(37) Hori, Y.; Takahashi, I.; Koga, O.; Hoshi, N. Electrochemical reduction of carbon dioxide at various series of copper single crystal electrodes. *J. Mol. Catal. A: Chem.* **2003**, *199*, 39.
(38) Iyengar, P.; Huang, J.; De Gregorio, G.; Gadiyar, C.; Buonsanti, R. Size dependent selectivity of Cu nano-octahedra catalysts for the electrochemical reduction of CO2 to CH4. *Chem. Commun.* **2019**, *55*, 8796.
(39) Loiudice, A.; Lobaccaro, P.; Kamali, E. A.; Thao, T.; Huang, B. H.; Ager, J. W.; Buonsanti, R. Tailoring Copper Nanocrystals towards C2 Products in Electrochemical CO2 Reduction. *Angew. Chem., Int. Ed.* **2016**, *55*, 5789.
(40) Huang, J.; Mensi, M.; Oveisi, E.; Mantella, V.; Buonsanti, R. Structural Sensitivities in Bimetallic Catalysts for Electrochemical CO2 Reduction Revealed by Ag−Cu Nanodimers. *J. Am. Chem. Soc.* **2019**, *141*, 2490.
(41) Manthiram, K.; Beberwyck, B. J.; Alivisatos, A. P. Enhanced electrochemical methanation of carbon dioxide with a dispersible nanoscale copper catalyst. *J. Am. Chem. Soc.* **2014**, *136*, 13319.
(42) Reske, R.; Mistry, H.; Behafarid, F.; Roldan Cuenya, B.; Strasser, P. Particle size effects in the catalytic electroreduction of CO_2 on Cu nanoparticles. *J. Am. Chem. Soc.* **2014**, *136*, 6978.
(43) Kim, C.; Dionigi, F.; Beermann, V.; Wang, X.; Moller, T.; Strasser, P. Alloy Nanocatalysts for the Electrochemical Oxygen Reduction (ORR) and the Direct Electrochemical Carbon Dioxide Reduction Reaction (CO2RR). *Adv. Mater.* **2019**, *31*, 1805617.
(44) Strasser, P.; Gliech, M.; Kuehl, S.; Moeller, T. Electrochemical processes on solid shaped nanoparticles with defined facets. *Chem. Soc. Rev.* **2018**, *47*, 715.
(45) Suter, S.; Haussener, S. Optimizing Mesostructured Silver Catalysts for Selective Carbon Dioxide Conversion into Fuels. *Energy Environ. Sci.* **2019**, *12*, 1668.
(46) Wang, Y.; Shen, H.; Livi, K. J. T.; Raciti, D.; Zong, H.; Gregg, J.; Onadeko, M.; Wan, Y.; Watson, A.; Wang, C. Copper Nanocubes for CO2 Reduction in Gas Diffusion Electrodes. *Nano Lett.* **2019**, *19*, 8461.
(47) Strach, M.; Mantella, V.; Pankhurst, J. R.; Iyengar, P.; Loiudice, A.; Das, S.; Corminboeuf, C.; van Beek, W.; Buonsanti, R. Insights into Reaction Intermediates to Predict Synthetic Pathways for Shape-Controlled Metal Nanocrystals. *J. Am. Chem. Soc.* **2019**, *141*, 16312.
(48) Wang, L.; Nitopi, S. A.; Bertheussen, E.; Orazov, M.; Morales-Guio, C. G.; Liu, X.; Higgins, D. C.; Chan, K.; Nørskov, J. K.; Hahn, C.; Jaramillo, T. F. Electrochemical Carbon Monoxide Reduction on Polycrystalline Copper: Effects of Potential, Pressure, and pH on Selectivity toward Multicarbon and Oxygenated Products. *ACS Catal.* **2018**, *8* (8), 7445.
(49) Ma, M.; Clark, E. L.; Dalsgaard, S.; Therkildsen, K. T.; Chorkendorff, I.; Seger, B. J. Insights into the Carbon Balance for CO2 Electroreduction on Cu using Gas Diffusion Electrode Reactor Designs. *Energy Environ. Sci.* **2020**, *13*, 977.
(50) Kim, D.; Kley, C. S.; Li, Y.; Yang, P. Copper nanoparticle ensembles for selective electroreduction of CO2 to C2−C3 products. *Proc. Natl. Acad. Sci. U. S. A.* **2017**, *114*, 10560.
(51) Mistry, H.; Behafarid, F.; Reske, R.; Varela, A. S.; Strasser, P.; Roldan Cuenya, B. Tuning Catalytic Selectivity at the Mesoscale via Interparticle Interactions. *ACS Catal.* **2016**, *6*, 1075.
(52) Huang, J.; Hörmann, N.; Oveisi, E.; Loiudice, A.; De Gregorio, G.; Andreussi, A.; Marzari, N.; Buonsanti, R. Potential-induced nanoclustering of metallic catalysts during electrochemical CO2 reduction. *Nat. Commun.* **2018**, *9*, 3117.

https://dx.doi.org/10.1021/acscatal.0c00297
ACS Catal. 2020, 10, 4854−4862

(53) Manthiram, K.; Surendranath, Y.; Alivisatos, A. P. Dendritic assembly of gold nanoparticles during fuel-forming electrocatalysis. *J. Am. Chem. Soc.* **2014**, *136*, 7237.
(54) Xiao, H.; Cheng, T.; Goddard, W. A.; Sundararaman, R. Mechanistic Explanation of the pH Dependence and Onset Potentials for Hydrocarbon Products from Electrochemical Reduction of CO on Cu (111). *J. Am. Chem. Soc.* **2016**, *138*, 483.
(55) Varela, A. S.; Kroschel, M.; Reier, T.; Strasser, P. Controlling the selectivity of CO2 electroreduction on copper: The effect of the electrolyte concentration and the importance of the local pH. *Catal. Today* **2016**, *260*, 8.
(56) Verma, S.; Hamasaki, Y.; Kim, C.; Huang, W.; Lu, S.; Jhong, H.-R. M.; Gewirth, A. A.; Fujigaya, T.; Nakashima, N.; Kenis, P. J. A. Insights into the Low Overpotential Electroreduction of CO2 to CO on a Supported Gold Catalyst in an Alkaline Flow Electrolyzer. *ACS Energy Lett.* **2018**, *3*, 193.
(57) Liu, K.; Smith, W. A.; Burdyny, T. Introductory Guide to Assembling and Operating Gas Diffusion Electrodes for Electrochemical CO2 Reduction. *ACS Energy Lett.* **2019**, *4*, 639.
(58) Moosavi, S. M.; Niffeler, M.; Gostick, J.; Haussener, S. Transport characteristics of saturated gas diffusion layers treated with hydrophobic coatings. *Chem. Eng. Sci.* **2018**, *176*, 503.

https://dx.doi.org/10.1021/acscatal.0c00297
ACS Catal. 2020, 10, 4854−4862